Science
AAAS

Supplementary Materials for

Structure of the Yeast Mitochondrial Large Ribosomal Subunit

Alexey Amunts*, Alan Brown*, Xiao-chen Bai*, Jose L. Llácer *, Tanweer Hussain, Paul Emsley, Fei Long, Garib Murshudov, Sjors H.W. Scheres[†], V. Ramakrishnan[†]

MRC Laboratory of Molecular Biology, Francis Crick Avenue, Cambridge CB2 0QH, United Kingdom

*These authors contributed equally

[†]To whom correspondence should be addressed at scheres@mrc-lmb.cam.ac.uk or ramak@mrc-lmb.cam.ac.uk

This PDF file includes:

Materials and Methods
Figs. S1 to S10
Tables S1 to S3

Materials and Methods

Isolation of mitochondria

Saccharomyces cerevisiae were grown aerobically in YPG media (1% yeast extract, 2% peptone, 3% glycerol) until an OD_{600nm} of 1.5 was reached. The cells were pelleted by centrifugation at 4,500*g* for 10 min and washed with distilled water. Mitochondria were isolated as previously described (*1*). The yeast pellet was resuspended in pre-warmed DTT buffer (100 mM Tris-HCl pH 9.3, 10 mM DTT) and incubated at 30°C for 30 min. The cells were collected by centrifugation at 3,500*g* for 10 min and washed with Zymolyase buffer (20 mM K_2HPO_4-HCl pH 7.5, 1.2 M sorbitol). The pellet was resuspended in Zymolyase buffer again to OD_{600nm} 0.6 and 1 mg Zymolyase-100T (MP Biomedicals, LLC) was added per gram wet weight, shaken slowly at 30°C for 60 min. Spheroplasts were harvested by centrifugation at 4,000*g* for 15 min and washed. Pellets were resuspended in homogenization buffer (20 mM Hepes-KOH pH 7.45, 0.6 M sorbitol, 1 mM EDTA) and lysed with 15 strokes in a 200 ml glass homogenizer. Lysis was confirmed by light microscopy. Cell debris and nuclei were separated at 4500*g* for 20 min. Crude mitochondria were collected at 13,000*g* for 25 min and further purified on sucrose gradient in SEM buffer (250 mM sucrose, 20 mM Hepes-KOH pH 7.5, 1 mM EDTA). Mitochondria samples were pooled and stored at -80ºC.

Purification of mitoribosomes

4 volumes of Lysis buffer (25 mM Hepes-KOH pH 7.5, 100 mM KCl, 25 mM MgOAc, 1.7% Triton X-100, 2 mM DTT) were added to purified mitochondria and incubated for 15 min in 4°C. The membranes were then separated by two centrifugations of 30,000*g* for 20 min each. The supernatant was loaded on a 1 M sucrose cushion in buffer: 20 mM Hepes-KOH pH 7.5, 100 mM KCl, 20 mM MgOAc, 1% Triton X-100, 2 mM DTT. The pellet was resuspended and incubated with 0.5 mM puromycin at 4°C for 30 min. The resuspended pellet was then loaded on 10%-30% sucrose gradient in the same buffer without Triton X-100 and run for 16 h at 80,000*g*. Fractions corresponding to mitoribosomes were collected and sucrose removed by buffer exchange, also in the same buffer.

Electron microscopy

Aliquots of 3 µl of purified mitochondrial ribosomes at a concentration of ~40 nM (0.15 mg/ml) were incubated for 30 s on glow-discharged holey carbon grids (Quantifoil R2/2), onto which a home-made continuous carbon film (estimated to be ~30 Å thick) had previously been deposited. Grids were blotted for 2.5 s in 100% ambient humidity and flash frozen in liquid ethane using an FEI Vitrobot. Grids were transferred to an FEI Titan Krios electron microscope that was operated at 300 kV. Images were recorded manually during three non-consecutive days on a back-thinned FEI Falcon II detector at a calibrated magnification of 104,478 (yielding a pixel size of 1.34 Å). All pictures that showed signs of significant astigmatism or drift were discarded during data collection. An in-house built system (*2*) was used to intercept the videos from the detector at a rate of 17 frames for the 1 s exposures. Defocus values in the final data set ranged from 1.2-4.7 µm.

Image processing

We used the Swarm tool in the e2boxer.py program of EMAN2 (*3*) for semi-automated selection of 135,949 particles from 1,030 micrographs. Contrast transfer function parameters were estimated using CTFFIND3 (*4*). All 2D and 3D classifications and refinements were performed using RELION (*5*). We used reference-free 2D class averaging to discard bad particles, and initiated 3D refinements with a 60 Å low-pass filtered cryo-EM reconstruction of the yeast cytoplasmic 80S ribosome (EMD-2275). Mitochondrial 74S

ribosomes and 54S subunits were separated from cytoplasmic 80S ribosomes using 3D classification with 6 classes and an angular sampling of 7.5° (Fig. S1). The resulting classes corresponding to mitochondrial 74S ribosomes and 54S subunits contained 38,955 and 25,184 particles, respectively. Statistical movie processing (*2*) of all 74S particles yielded a map with an overall resolution of 3.6 Å. Excellent density in the 54S subunit part of this map allowed for initial model building. However, the presence of distinct relative orientations of the large and small subunits in the data set resulted in much poorer density for the small subunit. Attempts to further classify this structural heterogeneity did not yield maps of sufficient quality to generate reliable (*de novo*) atomic models in the 39S part of the map.

The density for the large subunit was further improved by combining the 74S and 54S particles in a subsequent 3D refinement, where a mask that only included the large subunit was applied to the reference at every iteration. Statistical movie processing of 47,124 selected 74S and 54S particles yielded a final map with an overall resolution of 3.2 Å. Local resolution estimation using the ResMap program (*6*) revealed that the entire core of the large subunit is resolved at resolutions beyond 3 Å, whereas areas of density for structurally heterogeneous extensions at the periphery of the subunit are significantly worse (Fig. S2).

For statistical movie processing, we used running averages of five movie frames; a standard deviation of 1° for the priors on the Euler angles; and a standard deviation of 1 pixel for the translations. Reported resolutions are based on the gold-standard FSC=0.143 criterion (*7*), and we corrected for the effects of a soft mask on the FSC curve using high-resolution noise substitution (*8*). Prior to visualization, all density maps were corrected for the modulation transfer function (MTF) of the detector, and then sharpened by applying a negative B-factor (of -90 $Å^2$) that was estimated using automated procedures (*9*).

Model building and refinement

Our cryo-EM maps were of sufficient quality to allow us to appropriate model building and refinement tools designed for macromolecular crystal structures to solve and refine the structure of the mitochondrial ribosome. Initially, the structure of the *Thermus thermophilus* 70S ribosome large subunit (PDB ID: 3V2D) was placed into the density using rigid-body docking. As the highest resolution structure of a prokaryotic ribosome, this was used as our reference model for building and refining. Proteins L18, L20, L25 and 5S rRNA were removed as they have no homologs in the yeast mitochondrial ribosome.

The secondary structure prediction for *S. cerevisiae* 21S rRNA (GenBank ID: AJ011856) was obtained from the Comparative RNA Website (*10*). To guide matching of helices between the predicted secondary structure and the prokaryotic rRNA tertiary structure, the tertiary structure-derived secondary structure of *T. thermus* 23S rRNA was used (*11*). Conserved rRNA helices were extracted from globally docked *T. thermus* 23S rRNA structure and to overcome local differences in helix positioning, starting coordinates were optimized by applying a set of random rotations and small translations that were subsequently rigid-body refined and scored based on density fit. The sequence and numbering of bases were then altered to that of *S. cerevisiae* 21S rRNA and modifications made when necessary. Regions that differed substantially from the bacterial structure and expansion segments were built *de novo* into the density using idealized RNA and connected to the homologous regions using RCrane (*12*).

Yeast mitochondrial ribosome protein sequences were obtained from UniProt (*13*). Homologous proteins were mutated to the yeast sequence and insertions and extensions built

into the density. For all ribosomal proteins of unknown structure, three-dimensional models were predicted using I-TASSER (*14*). From these models, a library of motifs and domains was generated with unstructured regions removed. The density map was fragmented into search maps with radii of 30-40 Å centered on regions of density not accounted for by homologous proteins or rRNA. MOLREP was used to perform rotational and translational searches for all molecules in the library against all search maps (*15*). This approach was successful in identifying the positions of mL44, mL49 and mL57. Remaining density was populated by the automated localization of idealized secondary structure elements (SSEs) that were subsequently connected by poly-alanine traces using Cα baton mode within Coot v.0.8 (*16*). The length and connectivity of SSEs were compared with predicted secondary structure patterns to unambiguously assign sequences. The positions of bulky sidechains were used both for determination and validation of the correct assignment. For model building, low-pass filtered and B-factor sharpened maps were instrumental in defining the correct path to follow, especially on the periphery of the mitoribosome.

The model-building tools in Coot were modified in a number of ways to assist in the building of the mitoribosome from an EM map as follows. 1. The helix and strand fitting algorithms were tuned to EM maps which due to the large container box have a large region of zero or near zero density values. 2. The jiggle-fit algorithm was extended from single residues to arbitrary residue selections (for example, whole chains) with the addition of a computationally efficient atom-center scoring system for generation of candidate solutions. 3. To assist with molecular replacement with MOLREP, a tool was added to generate map fragments. Map density is "cut" from a particular position and radius in the ribosome map and translated to the origin. A spherical smoothing function was applied to the density. These density maps were then used for molecular replacement searches. Model morphing was achieved by cycling robust local averaging of chain fragment transformations. 4. Model morphing is undertaken as a 2-step process: first the shifts are generated by local (by default) 5-residue rigid-body transformations (associated with the central residue). The residues in the local environment (with a user-selectable radius) provide a set of transformations which are then robustly averaged to provide a transformation of the central residue. This is repeated for all residue (typically for a given chain). A number of cycles is needed for convergence. All these tools are available in the new version of Coot as both source code and binary files from the Coot web site (http://www2.mrc-lmb.cam.ac.uk/personal/pemsley/coot/).

The structure factors (including phases) obtained from the Fourier transform of the experimental density were used as the target of restrained refinement of coordinates and B factors in REFMAC v.5.8 (*17*). As the phases are already well determined by cryo-EM, they are not refined during refinement. For refinement five Gaussian approximations for electron scattering factors were used ((*volume C, table 4.3.2.2 in 18*). Initially all proteins and rRNA were refined separately before refining as a single model. This was achieved by refining against a section of map defined by a mask that extended 3 Å outward from the model coordinates. For the first round of rRNA refinement, reference restraints were generated for the conserved sections using ProSMART (*19*). These reference restraints were subsequently removed to allow for differences. Throughout rRNA refinement, base pair (canonical and G:U wobble) and stacking restraints were used in REFMAC. These restraints were generated automatically using the program LIBG (Fei Long, unpublished, available from the author at flong@mrc-lmb.cam.ac.uk). Geometric errors introduced into the rRNA during model building were corrected using the ERRASER-PHENIX pipeline (*20*) .

For yeast mitoribosomal proteins with bacterial homologs, main-chain interatomic distance restraints were derived from the reference structure using ProSMART. For all proteins, ProSMART was also used to generate idealized helical restraints and hydrogen-bond restraints for β-sheets. These reference and secondary structure restraints were maintained throughout refinement. Ramachandran restraints were not applied during refinement to preserve backbone dihedral angles for validation.

The R-factor and average overall Fourier shell correlation of the model to map (FSC, defined in Table S2) were monitored during refinement as a measure of how well the model predicts the observed data. The Rfactor is calculated and presented to make the results comparable to existing crystallographic model quality statistics. The average overall FSC is the summation of the FSC correlation in each shell and has the advantages that it accounts for phases as well as amplitudes of structure factors and is less dependent on weighting such as B-factor sharpening or blurring.

The final structure was validated using MolProbity (*21*). For cross-validation against over-fitting we tested the ability of the model to retain predictive power at a resolution higher than that used for refinement (3.2 Å). The atom positions of the final model were randomly displaced by up to a maximum of 0.5 Å before a full refinement was performed using secondary structure, base pair and planarity restraints against a map reconstruction from half the data only. The FSC was then calculated for both the map against which it had been refined and the map from the other half of the data, up to a resolution of 2.75 Å. We observe a significant correlation (t-test for Pearson correlation) beyond the resolution used for refinement, demonstrating clear predictive power for the model and absence of over-fitting (Fig. S2D). The distribution of B factors in the final refined model agreed well with the local resolution (Figs. S2E, F).

The intra-ribosomal protein-protein interaction network was mapped as an approximate two-dimensional representation of the three-dimension organization of the proteins in the mitoribosome using CytoScape (*22*). Node sizes represent protein molecular weights calculated excluding predicted mitochondrial-targeting peptides. The edge thickness represents the buried surface area between proteins calculated using PISA (*23*).

A secondary structure diagram for the 21S rRNA was constructed by extracting base pairs from the model using DSSR (*24*), mapping these to the full nucleotide sequence, with secondary structure predicted for unbuilt regions using Mfold (*25*). The secondary structure diagram was drawn in VARNA (*26*) and finalized in Inkscape.

All figures were generated using *Coot* (*16*) and Raster3D (*27*), PyMOL (*28*) or Chimera (*29*). The PDB2PQR server and Adaptive Poisson-Boltzmann Solver were used to calculate electrostatic potential (*30*). To visualize the exit tunnel, HOLLOW (*31*) was used to fill the channel volume with dummy atoms defined on a 0.5 Å grid. An interior probe of 2.5 Å was used to explore the cavity and a probe of 15 Å used to roll over the surface to define depressions.

Table S1. Ribosomes from various domains of life

	Class I	Class II			Class III (Mitochondria)			
	Eukaryotes	Archaea	Bacteria	Chloroplast	Protists	Fungi	Plants	Animals
Sedimentation coefficient	80S	70S			50S-81S	67S-74S	78S	55S-60S
Mw (MDa)	3.3-4.5	2.3-2.6			2.2-3.2	3-3.3	~3.5	~2.7
rRNA (nt)	5100-7200	4500-4600			1800-4400	4900-5800	~5800	~2500
Proteins	79-81	54-58			44-66	75-80	63-68	77-81

Table S2. Refinement and model statistics

Data Collection	
Particles	47,124
Pixel size (Å)	1.34
Defocus range (μm)	1.2-4.7
Voltage (kV)	300
Electron dose (e- $Å^{-2}$)	25
Model composition	
Non-hydrogen atoms	111,292
Protein residues	6,825
RNA bases	2,733
Ligands (Zn^{2+}/Na^{+}/Mg^{2+})	2/1/110
Refinement	
Resolution (Å)	3.2
Map sharpening B-factor ($Å^2$)	-90
Average B factor ($Å^2$)	94.78
Rfactor*	0.248
Fourier Shell Correlation†	0.881
Rms deviations	
Bonds (Å)	0.006
Angles (°)	0.998
Validation (proteins)	
Molprobity score	2.59 (96th percentile)
Clashscore, all atoms	6.13 (100th percentile)
Good rotamers (%)	89.7
Ramachandran plot	
Favored (%)	92.0
Outliers (%)	1.6
Validation (RNA)	
Correct sugar puckers (%)	97.18
Good backbone conformations (%)	73.98

*Rfactor = $\Sigma||F_{obs}|-||F_{calc}| / \Sigma|F_{obs}|$

† $FSC_{overall} = \Sigma(N_{shell}\ FSC_{shell}) / \Sigma(N_{shell})$, where FSC_{shell} is the FSC in a given shell, N_{shell} is the number of 'structure factors' in the shell. $FSC_{shell} = \Sigma(F_{model}\ F_{EM})/(\sqrt{(\Sigma(|F|^2_{model}))}\ \sqrt{(\Sigma(F^2_{EM}))})$.

Table S3. Proteins of the yeast mitoribosome. Mitochondrial ribosomal proteins (MRPs) were named using a nomenclature system where proteins with a prefix "u" (for universal) are observed in all kingdoms of life, proteins with a prefix "b" are bacterial in origin and do not have a eukaryotic (or archaeal) homolog, and proteins with a prefix "m" are mitochondria-specific. Protein residues are numbered according to UniProt with built residues shown. Universally conserved proteins were superposed with the bacterial homolog and the number of aligned residues given. Mitochondria-specific proteins and protein extensions were compared to known structures in the PDB using PDBeFold (*32*) and Dali (*33*).

Yeast MRP	Old nomenclature	Systematic name	Ref.	Bacterial homolog	Human MRP	Mature polypeptide (range, amino acids)	Chain ID	Built residues	RMSD with bacterial homolog (Å), number of Cα superposed	Features and structural similarity to known domains (PDB code of closest structural homolog, RMSD, Cα residues superposed)
uL1	MRPL1	YDR116C	(*34*)	L1	MRPL1	1-285				
uL2	RML2	YEL050C	(*35*)	L2	MRPL2	44-393	B	79-214, 230-388	1.11, 267	Na/K ligand. NT extension at the subunits interface.
uL3	MRPL9	YGR220C	(*36*)	L3	MRPL3	20-269	C	21-269	1.18, 203	NT extension interacts helix 0-ES2
uL4	YML6	YML025C	(*37*)	L4	MRPL4	27-286	D	31-189, 200-279	2.03, 186	
uL5	MRPL7	YDR237W	(*37*)	L5		20-292	E	19-292	1.36, 176	Unlike bacterial L5 does not bind Zn; loop insertion extends into region vacated by 5S rRNA
uL6	MRPL6	YHR147C	(*37*)	L6		17-214	F	18-45, 48-79, 83-89, 92-134, 137-194, 196-212	1.33, 167	
bL12	MNP1	YGL068W	(*38*)	L7/L12	MRPL7	34-194				
bL9	MRPL50	YNR022C	(*34*)	L9	MRPL9	1-139	G	10-59	1.32, 39	Small NT extension contacts a 2-nucleotide extension of helix 75.
uL10	MRPL11	YDL202W	(*37*)	L10	MRPL10	32-249				
uL11	MRPL19	YNL185C	(*37*)	L11	MRPL11	74-158				
uL13	MRPL23	YOR150W	(*37*)	L13	MRPL13	5-163	H	2-149	1.25, 126	
uL14	MRPL38	YKL170W	(*37*)	L14	MRPL14	1-138	I	1-49, 63-138	0.89, 118	
uL15	MRPL10	YNL284C	(*37*)	L15	MRPL15	58-322	J	58-277	1.68, 72	
uL16	MRPL16	YBL038W	(*37*)	L16	MRPL16	42-232	K	38-232	1.31, 132	CT extension compensates for loss of 5S rRNA
uL17	MRPL8	YJL063C	(*34*)	L17	MRPL17	1-238	L	2-221, 230-238	1.15, 112	CT extension similar to KaiA circadian clock regulator (1R5Q, 2.76Å^2, 72). Also similar to lipid transfer proteins (1BE2, 3.36Å^2, 70). Extension located close to the bacterial

										peptide exit tunnel.
bL19	IMG1	YCR046C	(*34*)	L19	MRPL19	17-169	M	16-166	1.93, 98	NT extension interacts with helix 0–ES2.
bL21	MRPL49	YJL096W	(*37*)	L21	MRPL21	36-161	N	44-161	1.76, 98	
uL22	MRPL22	YNL177C	(*34*)	L22	MRPL22	26-309	O	86-89, 91-309	1.38, 110	NT extension helps block bacterial exit tunnel and forms the walls of the alternative one. Compensates the absence of rRNA helix 24.
uL23	MRP20 (MRPL41)	YDR405W	(*39*)	L23	MRPL23	46-263	P	55-261	1.98, 82	CT extension blocks bacterial exit tunnel and forms the walls of the alternative one.
uL24	MRPL40	YPL173W	(*37*)	L24	MRPL24	1-297	Q	2-56, 59-135, 148-163, 165-174, 177-297	1.36, 63	NT extension helps in blocking bacterial exit tunnel and forming the walls of the alternative one. CT extension covers a long distance through the surface connecting different parts of the 54S subunit and compensating the absence of bacterial helices 10, 15 and 16.
bL27	MRP7	YNL005C	(*34*)	L27	MRPL27	28-371	R	35-187, 190-330, 346-354, 357-371	1.04, 74	CT domain forms a novel fold that interacts with helix 82 ES2 and ES3
bL28	MRPL24	YMR193W	(*37*)	L28	MRPL28	22-258	S	22-39, 44-171	2.48, 64	
uL29	MRPL4	YLR439W	(*38*)	L29	MRPL47	15-319	T	15-188, 195-211, 222-239	1.77, 29	NT extension compensates in part the absence of helix 63
uL30	MRPL33	YMR286W	(*40*)	L30	MRPL30	1-86	U	2-83	0.87, 59	
bL31	MRPL36	YBR122C	(*34*)	L31		15-177	V	20-83	1.66, 37	
bL32	MRPL32	YCR003W	(*40*)	L32	MRPL32	72-183	W	72-183	1.82, 48	Zn binding
bL33	MRPL39	YML009C	(*40*)	L33	MRPL33	1-70	X	6-69	1.51, 46	CT extension stabilizes E-site tRNA. Contacts also helix 82-ES1.
bL34	MRPL34	YDR115W	(*34*)	L34	MRPL34	17-105	Y	61-105	0.75, 42	
bL35	YNL122C	YNL122C		L35	MRPL35	1-115	Z	54-115	1.21, 62	
bL36	RTC6	YPL183W-A	(*34*)	L36	MRPL36	1-93	0	56-93	0.67, 36	Zn binding
mL38	MRPL35	YDR322W	(*37*)		MRPL38	30-367	1	20-45, 53-90, 97-299, 303-367		Phosphatidylethanolamine binding protein (1WPX, 1.82Å^2, 166). Stabilizes helix 82-ES3.
mL40	MRPL28	YDR462W	(*37*)		MRPL40	27-147	2	34-146		Stabilizes helix 84-ES1.
mL41	MRPL27	YBR282W	(*34*)		MRPL41	17-146	3	17-107, 110-138, 140-145		Stabilizes helix 8-ES1.
mL43	MRPL51	YPR100W	(*34*)		MRPL43	1-140	4	2-139		Thioredoxin fold (2VIM, 2.10Å^2, 70). Binds predominantly to helix 46.

mL44	MRPL3	YMR024W	(*34*)	MRPL44	60-390	5	65-390	Ribonuclease III family (NT) with a double-stranded RNA binding motif at the CT (2NUE, 2.39Å^2, 134). Forms a heterodimer with mL57. Stabilizes helix 0-ES1/2.
mL46	MRPL17	YNL252C	(*37*)	MRPL46	20-281	6	23-116, 136-172, 176-183, 187-204, 207-219, 230-239, 252-280	Nudix hydrolase-like superfamily (CT) (4KTB, 2.08Å^2, 93). Stabilizes helix 82-ES4.
mL49	IMG2	YCR071C	(*34*)	MRPL49	39-146	7	41-146	Similar to eIF1 (2XZM, 3.1Å^2, 89). Predominantly interacts with helix 27.
mL50	MRPL13	YKR006C	(*40*)	MRPL50	76-264	8	81-122, 125-264	Acyl carrier superfamily (1X3O, 1.9Å^2, 70). NT stabilizes helix 3-ES1.
mL53	MRPL44	YMR225C	(*40*)	MRPL53	1-98			
mL54	MRPL37	YBR268W	(*40*)	MRPL54	25-105			
mL57	MRPL15	YLR312W-A	(*37*)		29-253	9	29-60, 63-126, 140-181, 183-224, 227-241	Ribonuclease III family (NT). (3O2R, 2.1Å^2, 143). Forms a heterodimer with mL44. Stabilizes helix 0-ES.
mL58	MRPL20	YKR085C	(*34*)		19-195	a	20-195	DNA binding-domain (1IJW, 2.2Å^2, 44). Stabilizes helix 0-ES2 and 44-ES3.
mL59	MRPL25	YGR076C	(*34*)		1-157	b	3-157	Novel fold. CT stabilizes helix 82-ES3.
mL60	MRPL31	YKL138C	(*34*)		13-131	c	14-131	Similar to transcription factor DksA2 (4IIJ, 2.9Å^2, 85). Stabilizes helix 38-ES1 and 44-ES1.
mL61	MRP49	YKL167C	(*39*)		1-137			
MHR1[†]	MHR1	YDR296W			1-226	d	2-148, 158-214	Similar to a hypothetical protein (1ZG2, 3.9Å^2, 64). NT stabilizes helix 54-ES3.

[†]MHR1 has previously been shown to be involved in homologous recombination in yeast; due to the possibility of dual roles in mitochondria we have maintained this name in our recommended nomenclature.

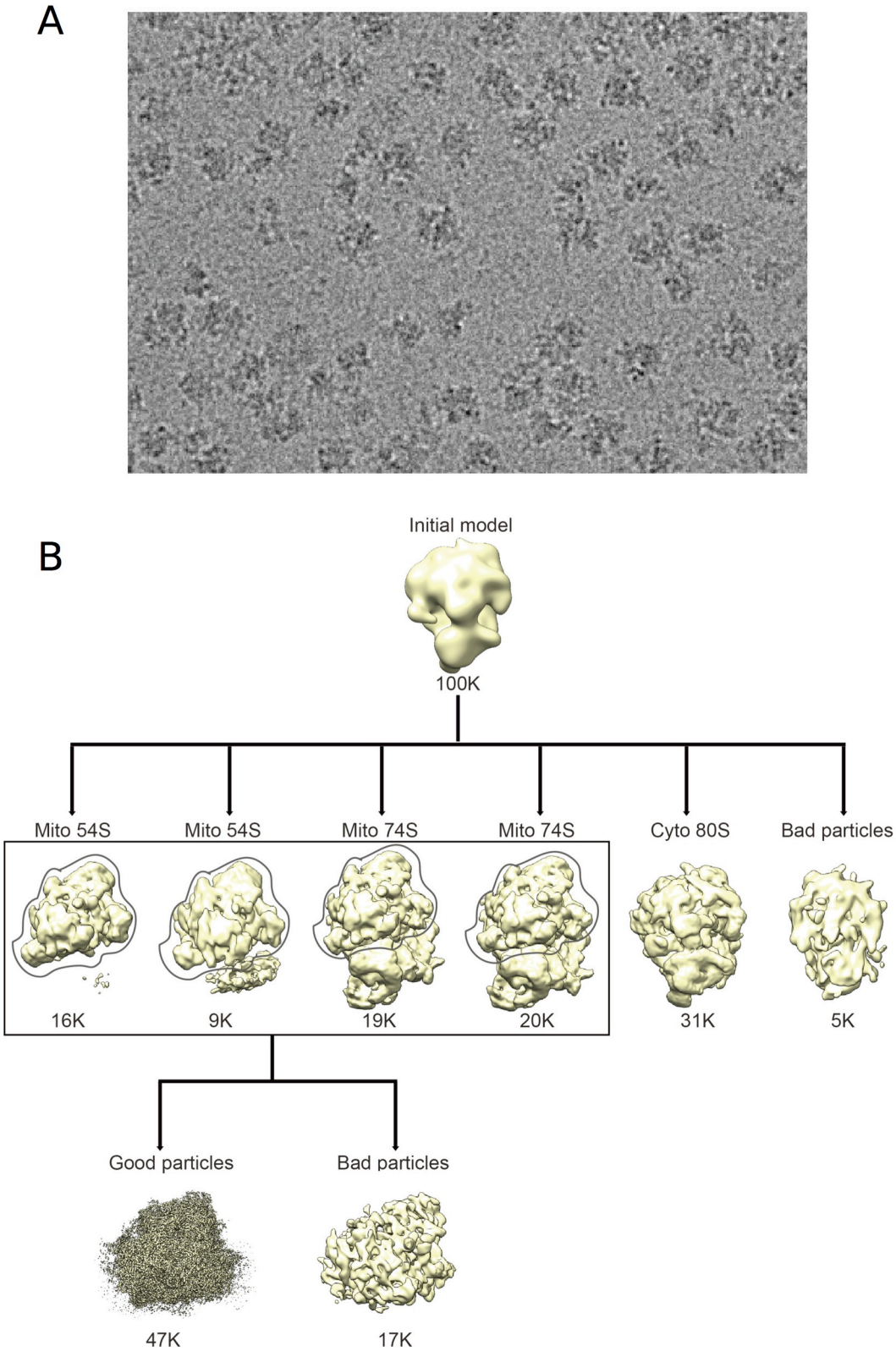

Fig. S1. Electron cryo-microscopy data and processing. A. Representative area of an electron micrograph. B. Maximum-likelihood classification scheme used to discard bad particles and separate cytoplasmic 80S ribosomes from mitochondrial 54S and 74S particles.

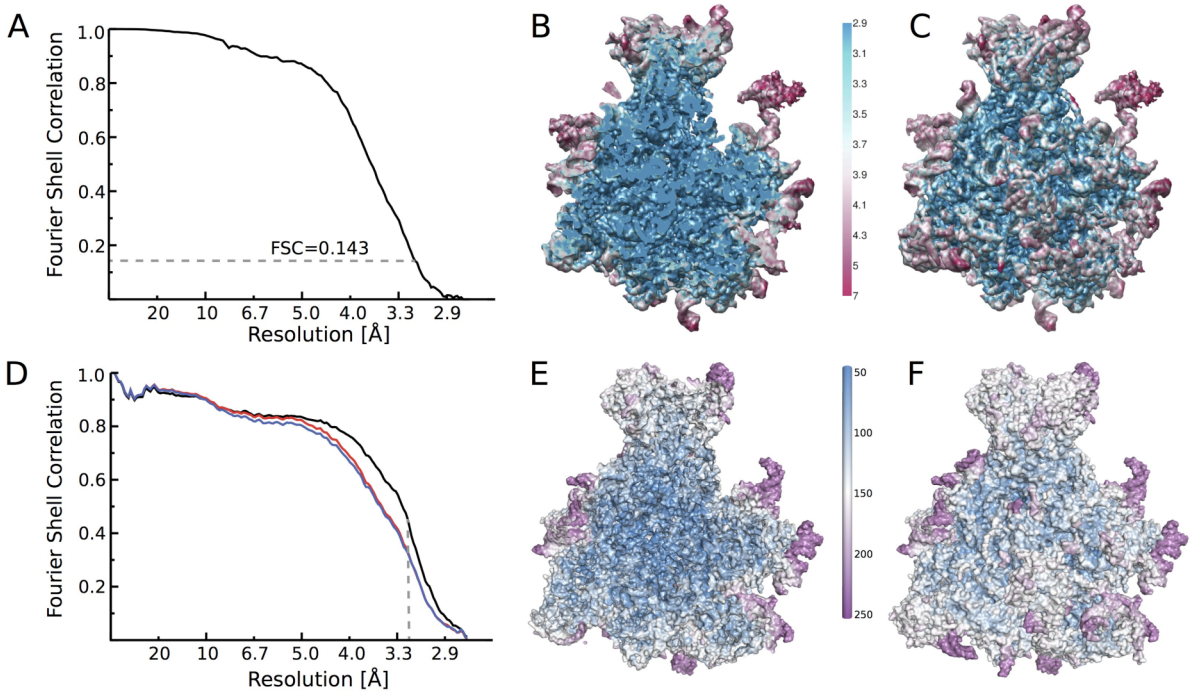

Fig. S2. Map and model quality. A. Gold-standard Fourier Shell Correlation (FSC) curve for the final structure. B. Cut-through view of the unsharpened final map colored according to local resolution (Å) (*6*). C. As in B, but for a surface view. D. FSC curves of the final model versus the map it was refined against (in black); of a model refined in the first of the two independent maps used for the gold-standard FSC versus that same map (in red); and of a model refined in the first of the two independent maps versus the second independent map (in blue). The vertical line at 3.2 Å indicates the highest resolution used in these model refinements. E. Cut-through view of the model colored according to the refined B-factors (in $Å^2$). F. As in E, but for a surface view.

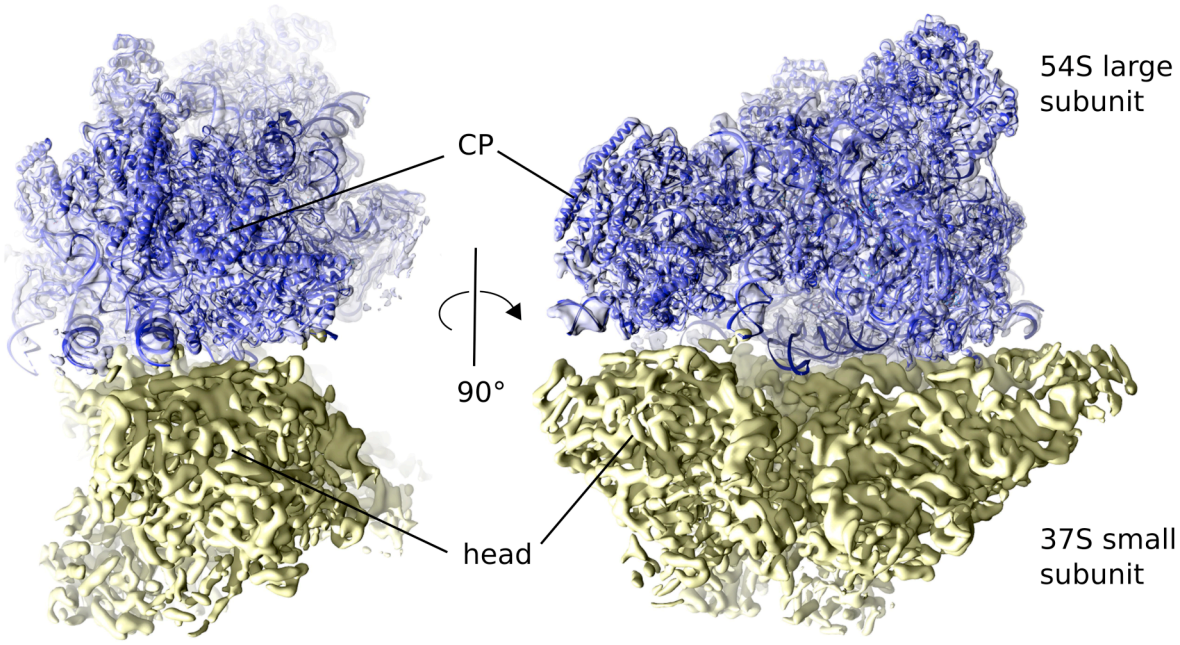

Fig. S3. Map reconstruction of the yeast 74S particle filtered to 7 Å. The 54S large subunit (blue) and 37S small subunit (yellow) of the yeast mitoribosome are shown in two orientations. The atomic model of the 54S subunit is shown in cartoon representation.

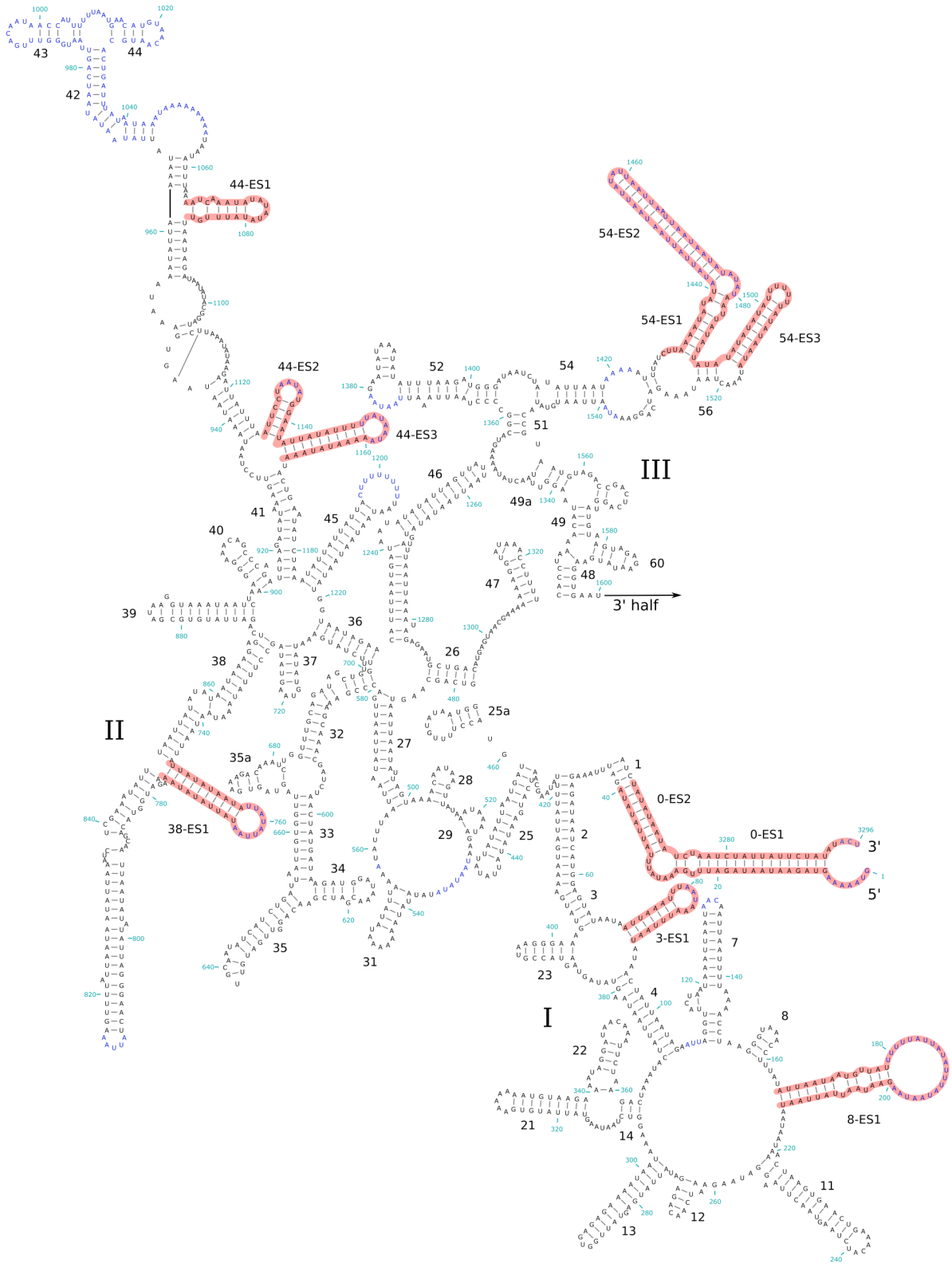

Fig. S4. Diagram of the secondary structure of the 5′ domain of 21S rRNA deduced directly from the structure. Expansion segments are shown in red. Secondary structure was predicted for unbuilt regions, shown in blue lettering. Domains are numbered in Roman numerals.

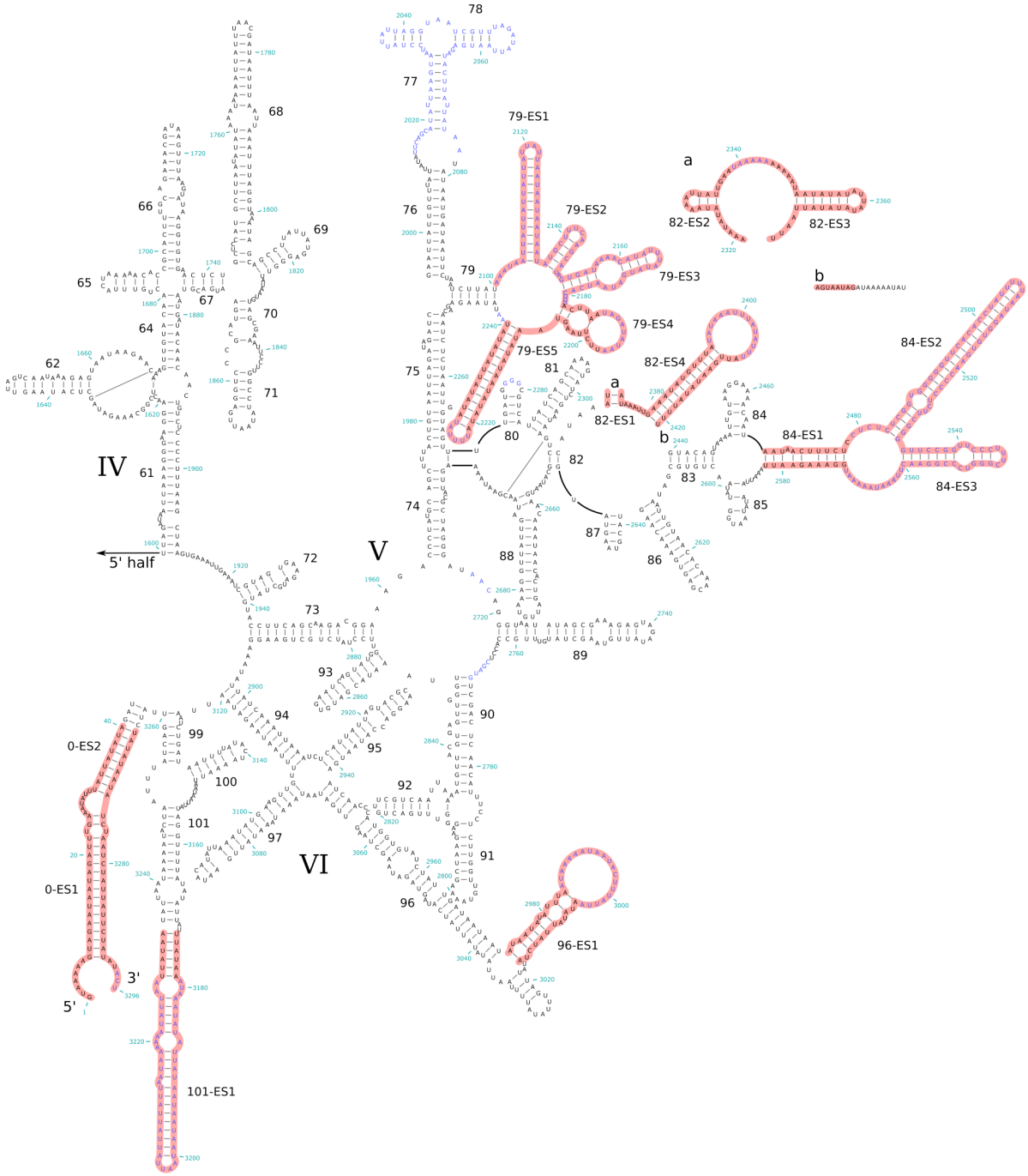

Fig. S5. Diagram of 3′ domain of 21S rRNA, similar to Fig. S4.

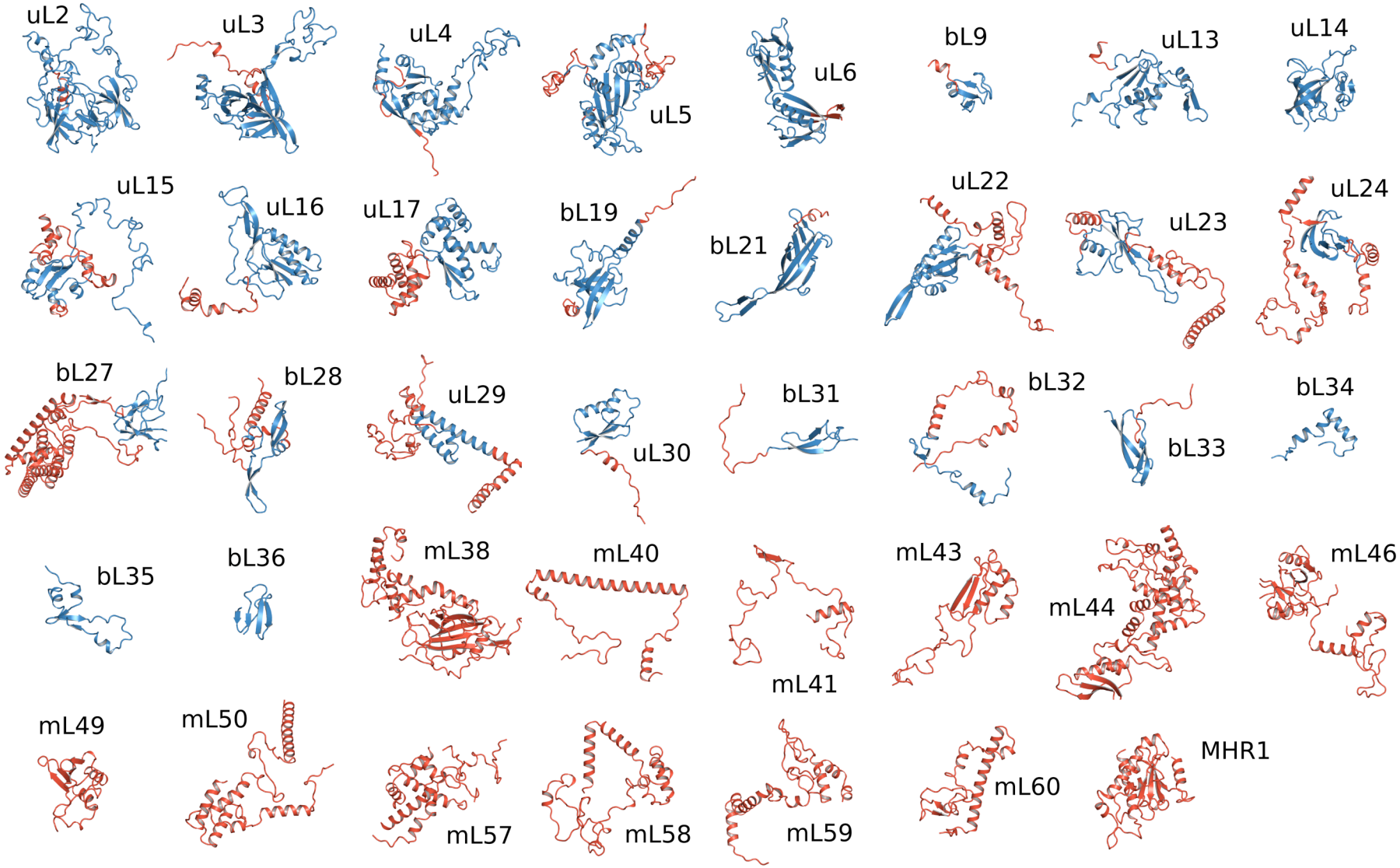

Fig. S6. Tertiary folds of the proteins built into the 54S subunit. Domains homologous to bacterial counterparts are shown in blue, and extensions and proteins unique to mitochondria are shown in red.

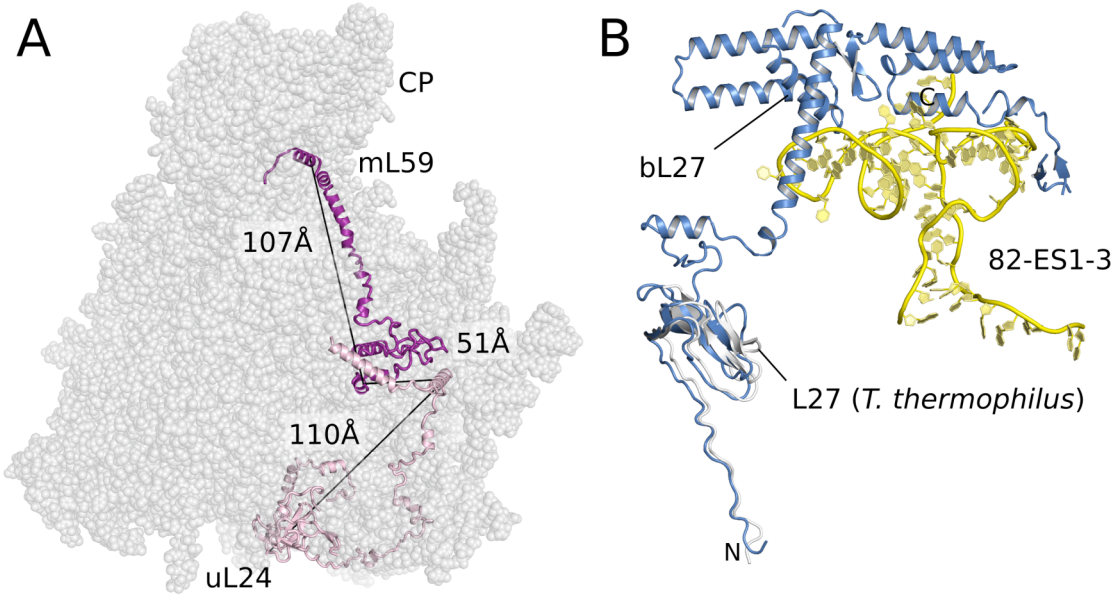

Fig. S7. Examples of protein extensions that result in long-range interactions. A. Two proteins that through their extensions span the entire diameter of the 54S subunit. B. The homologous part of bL27 superimposes well with bacterial L27 including the extension into the peptidyl transferase center at the N-terminus. But the much larger extension interacts with an expansion segment of 21S rRNA to form part of the central protuberance.

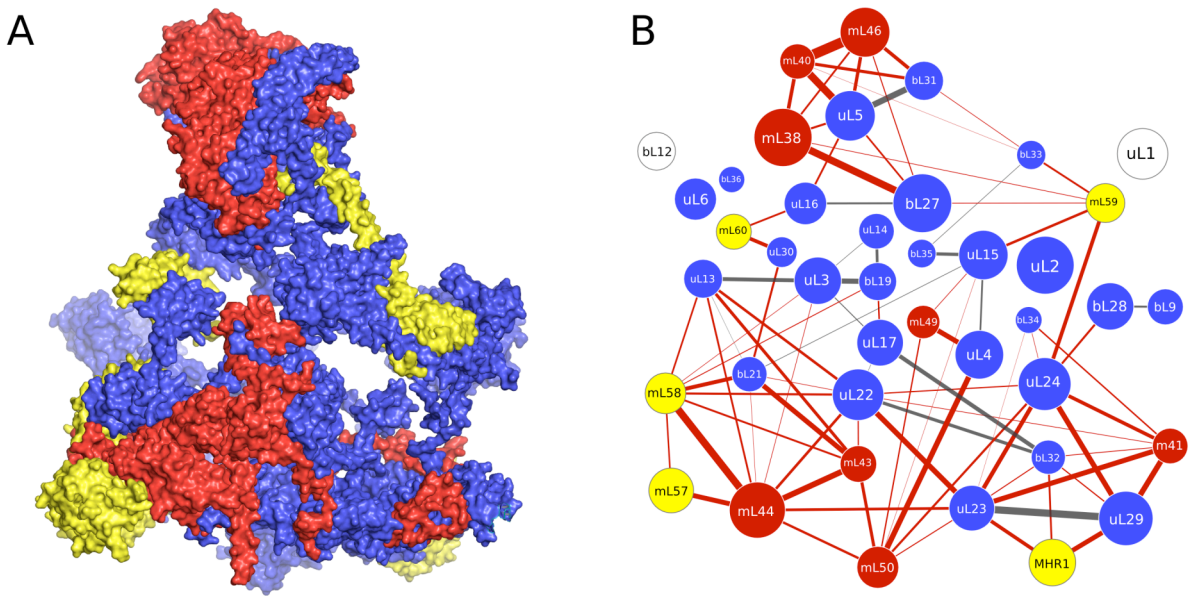

Fig. S8. Network of interactions of the ribosomal proteins. A. Surface representation showing extensive interactions of the ribosomal proteins. Conserved proteins are in blue, those common to other mitochondria in red and proteins specific to yeast mitochondria in yellow. B. Interaction network of the ribosomal proteins in the same colors as A. The node size represents the relative molecular mass of the protein and the edge thickness the solvent accessible surface buried in the interface. Interactions conserved with bacteria are shown in black, and mitochondria-specific interactions in red. bL12 and uL1 (white) were not built in the model and are shown for orientation purposes.

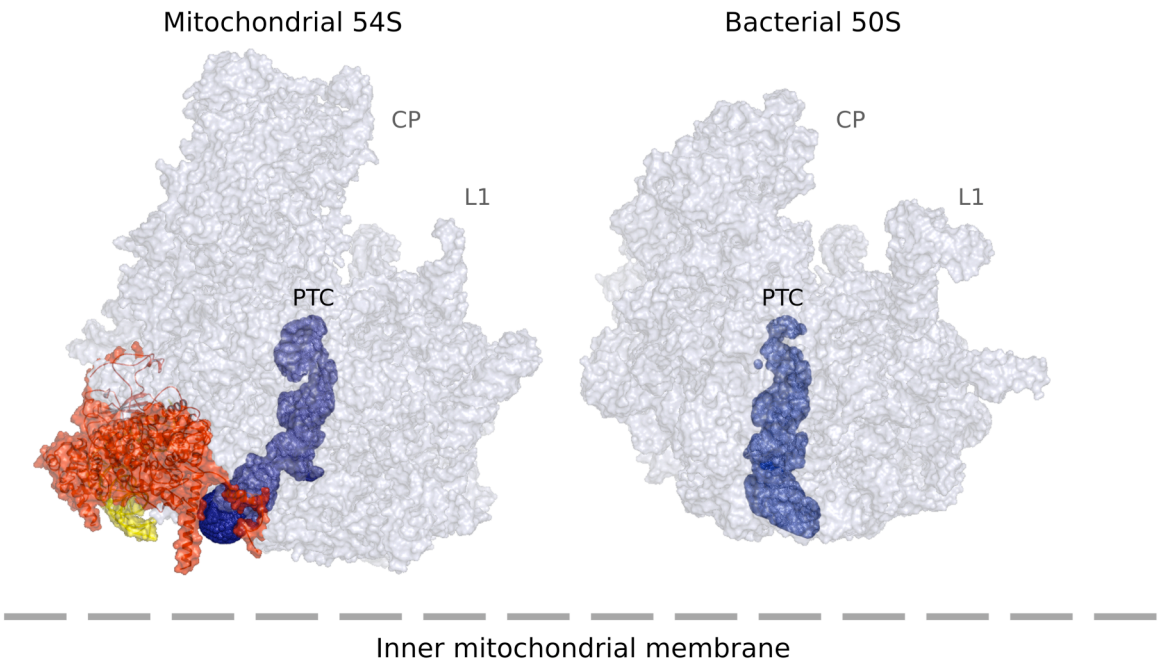

Fig. S9. Comparison between mitochondrial and bacterial exit tunnel path. Elements forming the mitochondria-specific membrane-facing protuberance are shown in red (proteins) and yellow (RNA).

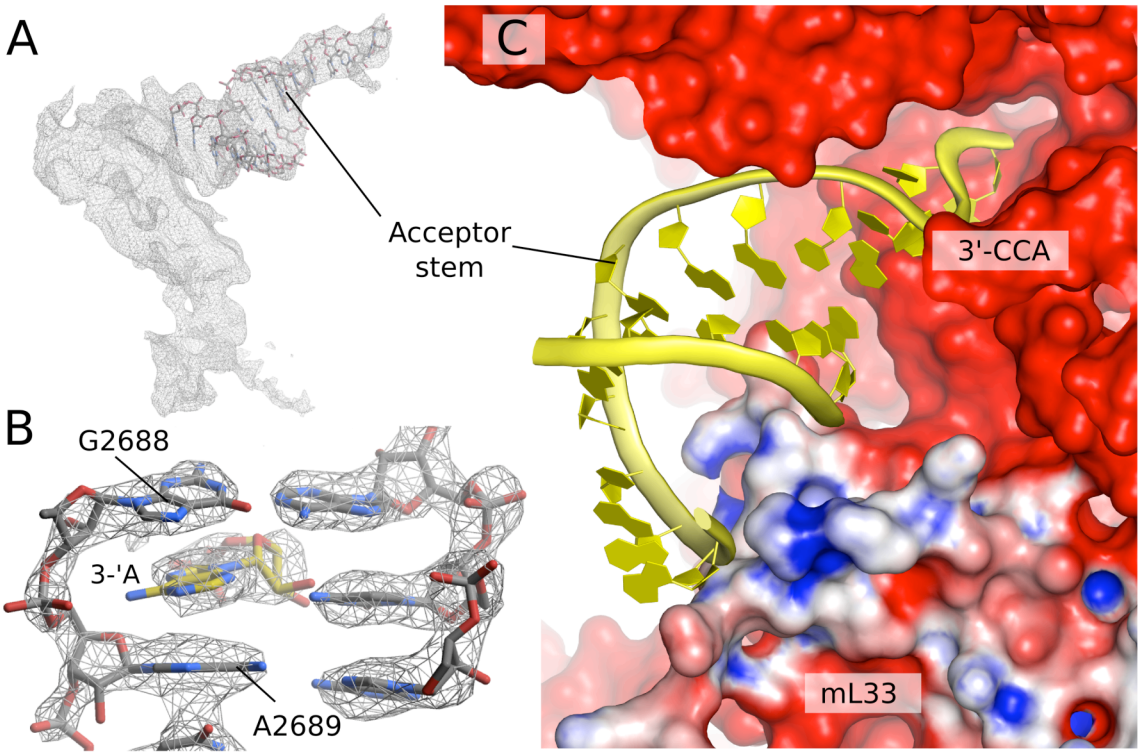

Fig. S10. The E site of the ribosome. A. Density for the endogenously co-purified E-site tRNA with the acceptor stem built. B. Intercalation of the terminal A76 between two purines of 21S rRNA in a manner identical to that previously seen in bacteria and archaea (see text). C. Overview of the E-site showing the extension to bL33 forming a new binding site for E-site tRNA that is unique to mitochondria.

References

1. C. Meisinger, N. Pfanner, K. N. Truscott, Isolation of yeast mitochondria. *Methods Mol Biol* **313**, 33 (2006).
2. X.-C. Bai, I. S. Fernandez, G. McMullan, S. H. Scheres, Ribosome structures to near-atomic resolution from thirty thousand cryo-EM particles. *eLife* **2**, e00461 (2013).
3. G. Tang *et al.*, EMAN2: an extensible image processing suite for electron microscopy. *J Struct Biol* **157**, 38 (2007).
4. J. A. Mindell, N. Grigorieff, Accurate determination of local defocus and specimen tilt in electron microscopy. *J Struct Biol* **142**, 334 (2003).
5. S. H. Scheres, RELION: implementation of a Bayesian approach to cryo-EM structure determination. *J Struct Biol* **180**, 519 (2012).
6. A. Kucukelbir, F. J. Sigworth, H. D. Tagare, Quantifying the local resolution of cryo-EM density maps. *Nat Methods* (2013).
7. S. H. Scheres, S. Chen, Prevention of overfitting in cryo-EM structure determination. *Nat Methods* **9**, 853 (2012).
8. S. Chen *et al.*, High-resolution noise substitution to measure overfitting and validate resolution in 3D structure determination by single particle electron cryomicroscopy. *Ultramicroscopy* **135**, 24 (2013).
9. P. B. Rosenthal, R. Henderson, Optimal determination of particle orientation, absolute hand, and contrast loss in single-particle electron cryomicroscopy. *J Mol Biol* **333**, 721 (2003).
10. J. J. Cannone *et al.*, The comparative RNA web (CRW) site: an online database of comparative sequence and structure information for ribosomal, intron, and other RNAs. *BMC bioinformatics* **3**, 2 (2002).
11. A. S. Petrov *et al.*, Secondary structure and domain architecture of the 23S and 5S rRNAs. *Nucleic Acids Research* **41**, 7522 (2013).
12. K. S. Keating, A. M. Pyle, RCrane: semi-automated RNA model building. *Acta crystallographica. Section D, Biological crystallography* **68**, 985 (2012).
13. U. Consortium, Update on activities at the Universal Protein Resource (UniProt) in 2013. *Nucleic Acids Research* **41**, D43 (2013).
14. A. Roy, A. Kucukural, Y. Zhang, I-TASSER: a unified platform for automated protein structure and function prediction. *Nature protocols* **5**, 725 (2010).
15. A. Vagin, A. Teplyakov, Molecular replacement with MOLREP. *Acta crystallographica. Section D, Biological crystallography* **66**, 22 (2010).
16. P. Emsley, B. Lohkamp, W. G. Scott, K. Cowtan, Features and development of Coot. *Acta crystallographica. Section D, Biological crystallography* **66**, 486 (2010).
17. G. N. Murshudov *et al.*, REFMAC5 for the refinement of macromolecular crystal structures. *Acta crystallographica. Section D, Biological crystallography* **67**, 355 (2011).
18. E. E. Prince, Mathematical, physical and chemical tables. Online edition. *International tables for crystallography* **100**, (2006).
19. R. A. Nicholls, F. Long, G. N. Murshudov, Low-resolution refinement tools in REFMAC5. *Acta crystallographica. Section D, Biological crystallography* **68**, 404 (2012).
20. F.-C. Chou, P. Sripakdeevong, S. M. Dibrov, T. Hermann, R. Das, Correcting pervasive errors in RNA crystallography through enumerative structure prediction. *Nature methods* **10**, 74 (2013).
21. V. B. Chen *et al.*, MolProbity: all-atom structure validation for macromolecular crystallography. *Acta crystallographica. Section D, Biological crystallography* **66**, 12

(2009).
22. P. Shannon *et al.*, Cytoscape: a software environment for integrated models of biomolecular interaction networks. *Genome Res* **13**, 2498 (2003).
23. E. Krissinel, K. Henrick, Inference of macromolecular assemblies from crystalline state. *Journal of Molecular Biology* **372**, 774 (2007).
24. X.-J. Lu, W. K. Olson, 3DNA: a versatile, integrated software system for the analysis, rebuilding and visualization of three-dimensional nucleic-acid structures. *Nature protocols* **3**, 1213 (2008).
25. M. Zuker, Mfold web server for nucleic acid folding and hybridization prediction. *Nucleic Acids Res* **31**, 3406 (2003).
26. K. Darty, A. Denise, Y. Ponty, VARNA: Interactive drawing and editing of the RNA secondary structure. *Bioinformatics* **25**, 1974 (2009).
27. E. A. Merritt, D. J. Bacon, Raster3D: photorealistic molecular graphics. *Methods Enzymol* **277**, 505 (1997).
28. W. L. DeLano, The PyMOL molecular graphics system. (2002).
29. E. F. Pettersen *et al.*, UCSF Chimera--a visualization system for exploratory research and analysis. *J Comput Chem* **25**, 1605 (2004).
30. S. Unni *et al.*, Web servers and services for electrostatics calculations with APBS and PDB2PQR. *Journal of computational chemistry* **32**, 1488 (2011).
31. B. K. Ho, F. Gruswitz, HOLLOW: generating accurate representations of channel and interior surfaces in molecular structures. *BMC Struct Biol* **8**, 49 (2008).
32. E. Krissinel, K. Henrick, Secondary-structure matching (SSM), a new tool for fast protein structure alignment in three dimensions. *Acta Crystallogr D Biol Crystallogr* **60**, 2256 (2004).
33. L. Holm, P. Rosenstrom, Dali server: conservation mapping in 3D. *Nucleic Acids Res* **38**, W545 (2010).
34. X. Gan *et al.*, Tag-mediated isolation of yeast mitochondrial ribosome and mass spectrometric identification of its new components. *European Journal of Biochemistry* **269**, 5203 (2002).
35. C. Pan, T. L. Mason, Functional analysis of ribosomal protein L2 in yeast mitochondria. *J Biochem* **272**, 8165 (1997).
36. H. R. Graack, L. Grohmann, M. Kitakawa, K. L. Schäfer, V. Kruft, YmL9, a nucleus-encoded mitochondrial ribosomal protein of yeast, is homologous to L3 ribosomal proteins from all natural kingdoms and photosynthetic organelles. *European Journal of Biochemistry* **206**, 373 (1992).
37. M. Kitakawa *et al.*, Identification and characterization of the genes for mitochondrial ribosomal proteins of Saccharomyces cerevisiae. *European Journal of Biochemistry* **245**, 449 (1997).
38. H. R. Graack, B. Wittmann-Liebold, Mitochondrial ribosomal proteins (MRPs) of yeast. *Biochem J* **329**, 433 (1998).
39. K. Fearon, T. L. Mason, Structure and function of MRP20 and MRP49, the nuclear genes for two proteins of the 54 S subunit of the yeast mitochondrial ribosome. *J Biochem* **267**, 5162 (1992).
40. L. Grohmann *et al.*, Extended N-terminal sequencing of proteins of the large ribosomal subunit from yeast mitochondria. *FEBS Letters* **284**, 51 (1991).